The Astronomical Journal, 131:1119–1129, 2006 February

SCATTERING OF PLANETESIMALS BY A PLANET: FORMATION OF COMET CLOUD CANDIDATES

A. Higuchi[1] and E. Kokubo
Division of Theoretical Astronomy, National Astronomical Observatory of Japan, Mitaka, Tokyo 181-8588, Japan;
kokubo@th.nao.ac.jp

and

T. Mukai
Graduate School of Science and Technology, Kobe University, Kobe, Hyogo 657-8501, Japan; mukai@kobe-u.ac.jp
Received 2005 May 4; accepted 2005 October 16

ABSTRACT

We have investigated the first dynamical stage of comet cloud formation, the scattering of planetesimals by a planet. The orbits of planetesimals were calculated using circular restricted three-body formalism. We obtained the probabilities of the following results of scattering as functions of the orbital parameters of the planets and planetesimals: (1) collision with the planet, (2) escape from the planetary system, and (3) candidacy as a member of the comet cloud (planetesimals with large semimajor axes). We also derived simple empirical formulae for these probabilities that are accurate enough for order-of-magnitude estimation. We found that a planetesimal with an initial eccentricity of $e \gtrsim 0.4$ can escape from the planetary system or be a candidate for an element of the comet cloud due to scattering by a planet. As the energy range of the comet cloud is narrow, the probability of any planet producing escapers is always much higher than that of producing candidates. Using the probabilities and assuming a distribution of planetesimals, we obtained the efficiencies of collision, escape, and candidacy for a given planet. We applied the results to the solar system and found that, among the four giant planets, Jupiter is the planet most responsible for producing candidate elements of the Oort Cloud, as long as the inclination of planetesimals is constant or proportional to the reduced Hill radius of each planet.

Key words: Oort Cloud — solar system: formation

1. INTRODUCTION

The Oort Cloud is a spherical comet reservoir surrounding the solar system. It is generally accepted that it consists of more than 10^{12} comets, and its size is on the order of 10^4–10^5 AU (e.g., Weissman 1990; Dones et al. 2004). The existence of this comet reservoir was first proposed by Oort (1950). He suggested that planets scattered small bodies in the planetary region outward and that passing stars raised their perihelia out of the planetary region. There is general agreement that the Oort Cloud comets are the residual planetesimals of planet formation.

The standard scenario of the Oort Cloud formation consists of two dynamical stages: (1) giant planets raising the aphelia of planetesimals to the outer region of the solar system and (2) the Galactic tide, passing stars, and giant molecular clouds pulling their perihelia out of the planetary region. The first dynamical stage has been studied analytically by several authors (e.g., Safronov 1972; Weidenschilling 1975; Fernández 1978). Safronov (1972) estimated the ejection rate of planetesimals by the four giant planets and the relative importance of the planets for ejection and comet cloud formation. Using a Monte Carlo, Öpik-type code, Fernández (1978) calculated the probability of a planetesimal colliding with a planet, being ejected from the solar system, and having a near-parabolic orbit with close encounters with planets. Both Safronov (1972) and Fernández (1978) concluded that Jupiter and Saturn hardly contribute to the formation of the Oort Cloud, since their ejection rates are too high because of their large masses, and that Uranus and Neptune may have had important roles in the Oort Cloud formation.

The first direct numerical calculation of the overall formation of the Oort Cloud was performed by Duncan et al. (1987). Their calculation included the gravity of the four giant planets and passing stars, and the Galactic tide. They concluded that the density profile between 3000 and 50,000 AU is roughly a power law proportional to $r^{-3.5}$, where r is the heliocentric distance, and that the inner Oort Cloud (semimajor axis $<$20,000 AU) contains roughly 5 times as many comets as the outer Oort Cloud. Dones et al. (2006) performed a similar calculation but with small initial eccentricities of planetesimals, which may be more realistic initial conditions. Their calculations showed that planetesimals typical of those that form the Oort Cloud are originally from the Uranus-Neptune region and are given the last scattering by Saturn. Both papers deal only with the solar system and do not focus on the general properties of planet-planetesimal scattering. Therefore, their results cannot be applied to other planetary systems.

Tremaine (1993) first considered the formation of comet clouds in other planetary systems. Using the results of previous studies (e.g., Duncan et al. 1987; Heisler & Tremaine 1986), he derived a condition for comet cloud formation as a function of the mass (m_p) and semimajor axis of a planet (a_p). However, this condition is based on the previous calculations, which are applicable only to the solar system.

In order to construct a general theory of comet cloud formation applicable to general planetary systems, it is necessary to clarify the elementary processes with parameters other than those for the solar system. In this paper we investigate the first dynamical stage of comet cloud formation using numerical calculations. In the late stage of planet formation, the scattering of planetesimals by a planet results in one of four events: (1) collision with the planet, (2) escape from the planetary system, (3) survival in the planetary system, and (4) a fall onto the central

[1] Graduate School of Science and Technology, Kobe University, Kobe, Hyogo 657-8501, Japan; also at Research Fellow of the Japan Society for the Promotion of Science; higuchia@kobe-u.ac.jp.

star. We call the planetesimals with fates 1, 2, and 4 "colliders," "escapers," and "fallers," respectively. The fate 3 planetesimals with large semimajor axes, for example, larger than 3000 AU, are candidates to be elements of the comet cloud (hereafter "candidates"). We calculate the probabilities of producing colliders, escapers, and candidates by orbital integration using circular restricted three-body formalism. We integrate the orbits of the planetesimals for one Kepler period to evaluate the probability for one encounter. The ratios of these fates depend on the parameters of the planetary system, i.e., the orbital elements of the planetesimals and the orbital elements and mass of the relevant planet. We investigate the dependence of the ratios on these parameters. We also present simple and useful empirical fitting formulae for these probabilities.

The outline of this paper is as follows: We describe the numerical method, model, and initial conditions in § 2. In § 3 we present the results for the probabilities of colliders, escapers, and candidates. We derive empirical fitting formulae of the probabilities in § 4. In § 5, using the probabilities, we estimate the efficiencies of planets for producing colliders, escapers, and candidates and apply the results to the solar system. Section 6 is devoted to a summary and discussion.

2. METHOD OF CALCULATION

2.1. *Model and Initial Conditions*

We consider a star-planet-planetesimal three-body problem in which a planetesimal is treated as a massless particle. We consider planets of $a_p = 1, 5, 10$, and 30 AU and $m_p = 0.1m_J, 0.3m_J$, $1m_J$, $3m_J$, and $10m_J$, where $m_J \equiv 0.001m_*$ and m_* is the mass of the star, which is set as $m_* = 1\ M_\odot$. The orbit of the planet is assumed to be circular. We set the densities of the planet and star as 1 g cm^{-3}.

We set up an initial planetesimal disk that consists of planetesimals and a planet. All the planetesimals have the same eccentricity e and inclination i. The range of e is from 0.1 to 0.9 with an interval of 0.1, and the range of i is from 0 to 0.1 rad with an interval of 0.01. The semimajor axes of the planetesimals a are uniformly distributed over the planetesimal disk; in other words, the surface number density of planetesimals is proportional to a^{-1}. We call the region of a where the coplanar orbits of the planet and a planetesimal cross the "orbit-crossing region." The inner and outer edges of the orbit-crossing region for unperturbed orbits are $a_{\min} = a_p/(1+e)$ and $a_{\max} = a_p/(1-e)$, respectively, where a_p is the semimajor axis of the planet. We distribute planetesimals in a range wider than the orbit-crossing region, since gravitational focusing of the planet is effective. The argument of the perihelion ω, the longitude of the ascending node Ω, and the mean anomaly l of the planetesimals are distributed randomly. In the disk, a ring in a with a width of 1 AU contains 10^6 or 10^7 planetesimals. The initial disk parameters are summarized in Table 1.

TABLE 1
List of the Initial Model Parameters

	Planetesimal		Planet	
Case	e	i (rad)	a_p (AU)	m_p/m_J
0	0.1–0.9	0.05	5	1
1	0.1–0.9	0	5	1
2	0.1–0.9	0.01	5	1
3	0.1–0.9	0.02	5	1
4	0.1–0.9	0.03	5	1
5	0.1–0.9	0.04	5	1
6	0.1–0.9	0.06	5	1
7	0.1–0.9	0.07	5	1
8	0.1–0.9	0.08	5	1
9	0.1–0.9	0.09	5	1
10	0.1–0.9	0.1	5	1
11	0.1–0.9	0	1	1
12	0.1–0.9	0.05	1	1
13	0.1–0.9	0	10	1
14	0.1–0.9	0.05	10	1
15	0.1–0.9	0	30	1
16	0.1–0.9	0.05	30	1
17	0.1–0.9	0	5	0.1
18	0.1–0.9	0.05	5	0.1
19	0.1–0.9	0	5	0.3
20	0.1–0.9	0.05	5	0.3
21	0.1–0.9	0	5	3
22	0.1–0.9	0.05	5	3
23	0.1–0.9	0	5	10
24	0.1–0.9	0.05	5	10

2.2. *Integration Method*

The orbits of the planetesimals are integrated numerically using the fourth-order Hermite scheme (Makino & Aarseth 1992) with a hierarchical time step (Makino 1991). The equation of motion for a planetesimal is

$$\frac{d^2\boldsymbol{r}}{dt^2} = -Gm_*\frac{\boldsymbol{r}}{r^3} - Gm_p\left(\frac{\boldsymbol{r}-\boldsymbol{r}_p}{|\boldsymbol{r}-\boldsymbol{r}_p|^3} + \frac{\boldsymbol{r}_p}{r_p^3}\right), \tag{1}$$

where G is the gravitational constant, $\boldsymbol{r}_p$ is the heliocentric position of the planet, and $\boldsymbol{r}$ is the heliocentric position of the planetesimal. The last term of the right-hand side represents the indirect term.

We calculate the orbits of all the planetesimals for 1 Kepler period (T_K). During the orbit integration, if the separation between the planet and a planetesimal becomes smaller than the radius of the planet R_p or the heliocentric distance of the planetesimal becomes smaller than the radius of the central star R_*, the planetesimal is counted as a collider in the former and a faller in the latter. Orbital elements of planetesimals except colliders and fallers are checked after T_K. If the perihelion distance of the planetesimal is smaller than R_*, it is also counted as a faller. If the eccentricity of the planetesimal is larger than 1, it is counted as an escaper. A planetesimal with $a > a_{can}$ is counted as a candidate, where a_{can} is the minimum semimajor axis of a candidate for inclusion in the comet cloud. If the separation between the planet and a planetesimal after T_K is smaller than the Hill radius of the planet, $r_H = a_p(m_p/3m_*)^{1/3}$, we discard the planetesimal. This is just because its orbit changes a great deal due to strong interaction with the planet.

2.3. *Definitions of Probability and Efficiency*

We denote the probabilities of producing colliders, escapers, and candidates per T_K as P_{col}, P_{esc}, and P_{can}. Using these probabilities P, we define the efficiencies K of a planet. Efficiencies K_{col}, K_{esc}, and K_{can} represent the expected numbers of colliders, escapers, and candidates per unit time and are defined as

$$K = \int_{a_{in}}^{a_{out}} \frac{P}{T_K} n_s 2\pi a\, da, \tag{2}$$

where n_s is the surface number density of planetesimals, given as $n_s = n_1 a^\theta$, where n_1 is the reference surface number density

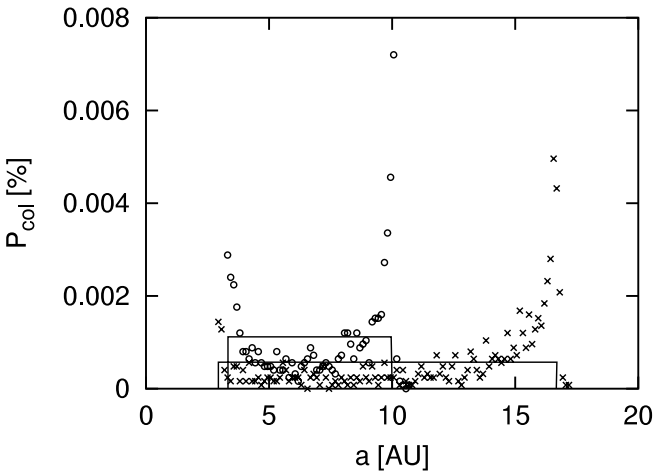

FIG. 1.—Probability $P_{\rm col}$ shown against a. Circles and crosses indicate $P_{\rm col}$ for $e = 0.5$ and 0.7, respectively, in the standard case (case 0) $[(i,\ a_p,\ m_p) = (0.05,\ 5\ {\rm AU},\ 1m_{\rm J})]$. The solid lines show the empirical fits.

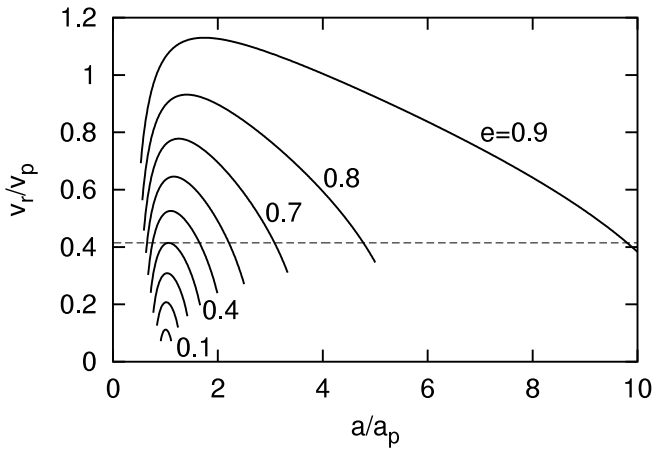

FIG. 2.—Relative velocities between a planetesimal and a planet scaled by v_p for $e = 0.1, 0.2, \ldots, 0.9$ and $i = 0.05$ are plotted against a scaled by a_p over the orbit-crossing region. The dashed line shows the critical velocity for escapers, $v_r^{\rm min}$.

at $a = 1$ AU, θ is the power-law index of the radial distribution, and $a_{\rm in}$ and $a_{\rm out}$ are the inner and outer edges of the planetesimal disk. In the present paper we do not show or discuss the probability and efficiency of becoming a faller.

3. PROBABILITIES

We numerically evaluate P and investigate its dependences on the parameters of the planetesimals and planets: a, e, i, a_p, and m_p. We show the results in order of $P_{\rm col}$, $P_{\rm esc}$, and $P_{\rm can}$. We refer to "case 0" as the standard case. For each P we first present the results of the standard case and the dependences on a and e. Next we show the dependences of P on the other parameters. The details of the parameter dependences are discussed in § 4.

3.1. *Collision with the Planet*

3.1.1. *Standard Case*

Figure 1 shows $P_{\rm col}$ against a for $e = 0.5$ in the standard case. In this case $a_{\rm min} = 3.3$ AU and $a_{\rm max} = 10$ AU. Collision takes place over the orbit-crossing region. The probability $P_{\rm col}$ has two peaks, one at each end of the region. The relative velocity between a planetesimal and the planet, v_r, explains this feature. In the two-body approximation, the collisional cross section of the planet is given by

$$\sigma_{\rm col} = \pi R_p^2 \left[1 + \left(\frac{V_{\rm esc}}{v_r}\right)^2\right], \qquad (3)$$

where $V_{\rm esc}$ is the surface escape velocity from the planet, given by $V_{\rm esc} = \left(2Gm_p/R_p\right)^{1/2}$. For the parameter range of this study, $v_r < V_{\rm esc}$ and gravitational focusing is effective (e.g., Kokubo & Ida 1996). Thus, the first term on the right-hand side of equation (3) can be neglected, and $\sigma_{\rm col}$ is proportional to v_r^{-2}. The number of collisions per $T_{\rm K}$ is proportional to $\sigma_{\rm col}$. The relative velocity for the unperturbed orbit of a planetesimal is given as

$$\left(\frac{v_r}{v_p}\right)^2 = 3 - 2\left[\frac{a}{a_p}\left(1 - e^2\right)\right]^{1/2} \cos i - \frac{a_p}{a}, \qquad (4)$$

where v_p is the Kepler velocity of the planet (e.g., Bertotti et al. 2003). Figure 2 shows v_r against a over the orbit-crossing region for $i = 0.05$. At both ends of the orbit-crossing region, v_r is smaller, and thus, $P_{\rm col}$ is larger. The real relative velocity may be slightly different from equation (4) because of planetary perturbation. However, the essential behavior of the real relative velocity is almost the same as that of equation (4).

Figure 1 also shows $P_{\rm col}$ for $e = 0.7$. In this case $a_{\rm min} = 2.9$ AU and $a_{\rm max} = 16.7$ AU. The overall shape of $P_{\rm col}$ is similar to that for $e = 0.5$. The region for collision expands and $P_{\rm col}$ decreases in its entirety as e increases.

3.1.2. *Parameter Dependences*

We compare $P_{\rm col}$ for different values of i, a_p, and m_p in Figure 3. The overall shape of $P_{\rm col}$ does not change with different i, a_p, and m_p. Figure 3*a* compares $P_{\rm col}$ for $i = 0.05$ and 0.07. The value of $P_{\rm col}$ decreases with increasing i. For $i = 0.07$, $P_{\rm col}$ is about two-thirds of $P_{\rm col}$ for $i = 0.05$. Figure 3*b* shows $P_{\rm col}$ for $a_p = 5$ and 10 AU. The orbit-crossing region shifts outward and expands with a_p, while $P_{\rm col}$ decreases with increasing a_p. For $a_p = 10$ AU, $P_{\rm col}$ is about half of $P_{\rm col}$ for $a_p = 5$ AU at the same a/a_p. Figure 3*c* shows $P_{\rm col}$ for $m_p = 1m_{\rm J}$ and $0.3m_{\rm J}$. The value of $P_{\rm col}$ increases with m_p. For $m_p = 0.3m_{\rm J}$, $P_{\rm col}$ is about one-fifth of $P_{\rm col}$ for $m_p = 1m_{\rm J}$.

3.2. *Escape from a Planetary System*

3.2.1. *Standard Case*

Figure 4 shows $P_{\rm esc}$ against a for $e = 0.7$ in the standard case, in which $a_{\rm min} = 2.9$ AU and $a_{\rm max} = 16.7$ AU. Escapers appear over most of the orbit-crossing region. In this region $P_{\rm esc}$ increases with a and suddenly drops before the outer edge of the region. This increase is also explained by v_r. The gravitational radius (impact parameter for 90° deflection) of a planet is given by $r_g = Gm_p/v_r^2$, which means that planetesimals with smaller v_r are easily scattered at large angles. The increase in $P_{\rm esc}$ with a may reflect that v_r decreases with increasing a for $a \gtrsim a_p$ (Fig. 2).

Figure 4 also shows $P_{\rm esc}$ for $e = 0.8$, where $a_{\rm min} = 2.8$ AU and $a_{\rm max} = 25$ AU. The overall shape of $P_{\rm esc}$ is similar to that for $e = 0.7$. The value of $P_{\rm esc}$ decreases with increasing e at constant a, although the maximum value of $P_{\rm esc}$ increases with e. The maximum value of $P_{\rm esc}$ for $e = 0.8$ is about twice that for $e = 0.7$.

We find that there are no escapers for $e \leq 0.3$. This is explained by a simple fly-by theory (e.g., Madonna 1997) based on the two-body approximation. By using $\boldsymbol{v}_r$ and $\boldsymbol{v}_p$, the velocity of a planetesimal is written as $v = |\boldsymbol{v}_p + \boldsymbol{v}_r|$. To escape from the planetary system, v needs to satisfy $v > v_{\rm esc}$, where $v_{\rm esc}$ is the local escape velocity $v_{\rm esc} = \left(2Gm_*/a_p\right)^{1/2} = \sqrt{2}v_p$. There is also

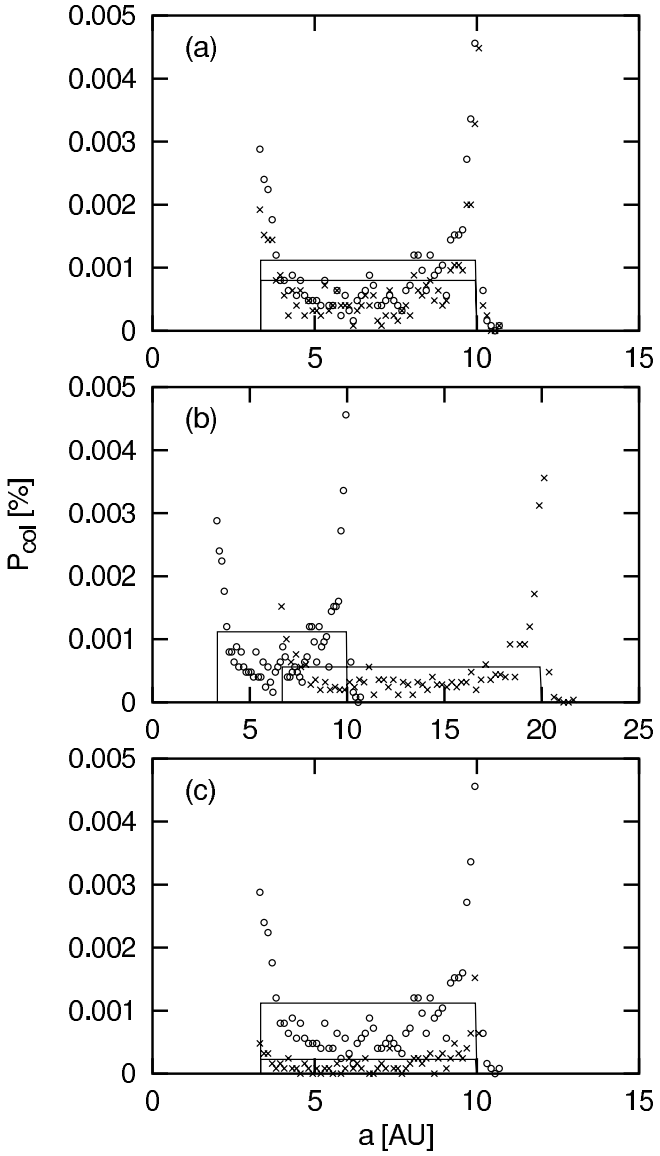

FIG. 3.—Probabilities P_{col} for $e = 0.5$ in the standard case (*circles*) and various other cases (*crosses*) shown against a. The crosses in (*a*), (*b*), and (*c*) indicate P_{col} in cases 6 ($i = 0.07$), 11 ($a_p = 10$ AU), and 14 ($m_p = 0.3m_J$), respectively. The solid lines show the empirical fits.

the minimum relative velocity v_r^{min} for escape derived from the fly-by theory. A planetesimal gains the largest additional velocity if it is scattered in the direction of the orbital motion of the planet. In this case v_r^{min} is given by $v_r^{min} = v_{esc} - v_p = (\sqrt{2} - 1)v_p$ (e.g., Fernández 1978). We plot v_r^{min} also in Figure 2. In the region where v_r is smaller than v_r^{min}, no planetesimals can escape. To satisfy the condition $v_r > v_r^{min}$, we need $e \gtrsim 0.4$. Thus, planetesimals initially with $e \lesssim 0.4$ cannot escape. Even for $e \gtrsim 0.4$, the condition is not satisfied near the end of the orbit-crossing region, and this explains the sudden drop in P_{esc} before the end of the region. However, in the case of large m_p, the simple fly-by theory is no longer valid. In case 16 there exist escapers even for $e \simeq 0$.

3.2.2. *Parameter Dependences*

In Figure 5 we compare P_{esc} for different values of i, a_p, and m_p. The overall shape of P_{esc}, the increase and sudden drop against a, does not change with different i, a_p, and m_p. Figure 5*a* compares P_{esc} for $i = 0.05$ and 0.07. Similarly to P_{col}, P_{esc} decreases with increasing i. The probability P_{col} for $i = 0.07$ is about two-thirds of P_{col} for $i = 0.05$. In Figure 5*b* we show P_{esc} for $a_p = 5$ and 10 AU. The orbit-crossing region shifts outward and expands with a_p, while P_{esc} at the peaks is almost the same, which may imply that P_{esc} is scaled by a/a_p. Figure 5*c* compares P_{esc} for $m_p = 1m_J$ and $0.3m_J$. Compared to P_{col}, P_{esc} increases steeply with m_p. The probability P_{esc} for $m_p = 0.3m_J$ is about 1/10 of P_{esc} for $m_p = 1m_J$.

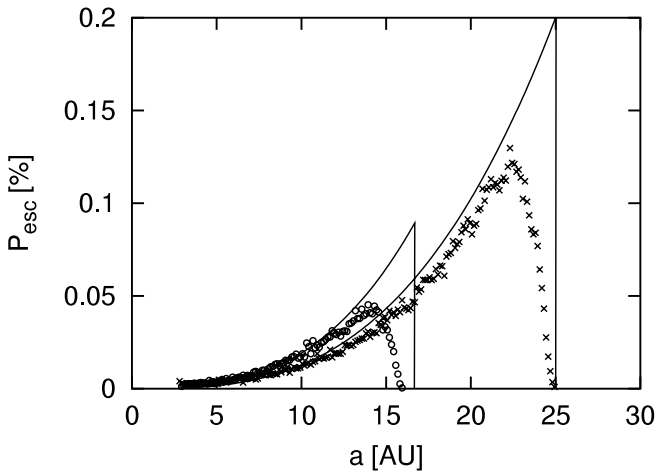

FIG. 4.—Probability P_{esc} shown against a. Circles and crosses indicate P_{esc} for $e = 0.7$ and 0.8, respectively, in the standard case [$(i, a_p, m_p) = (0.05, 5$ AU, $1m_J)$]. The solid curves show the empirical fits.

3.3. *Candidacy To Be a Member of a Comet Cloud*

3.3.1. *Standard Case*

Figure 6 shows P_{can} against a for $e = 0.7$ and in the standard case, in which $a_{min} = 2.9$ AU and $a_{max} = 16.7$ AU. We use $a_{can} = 3000$ AU, which corresponds to the inner edge of the inner Oort Cloud (Dones et al. 2006). Candidates appear almost over the orbit-crossing region. In this region P_{can} increases with a and suddenly drops before the end of the region. This behavior is similar to that of P_{esc} because large scattering is required for producing candidates, as well as escapers. However, the dependence on a is stronger than that of P_{esc}.

Figure 6 also shows P_{can} for $e = 0.8$. In this case $a_{min} = 2.8$ AU and $a_{max} = 25$ AU. Similarly to P_{esc}, the value of P_{can} decreases with increasing e at constant a, and the maximum value of P_{can} increases with e. The maximum value for $e = 0.8$ is about 3 times that for $e = 0.7$. There are no candidates for $e \leq 0.3$. It should be noted that P_{can} is always much smaller than P_{esc}.

3.3.2. *Parameter Dependences*

In Figure 7 we show P_{can} for a variety of parameters including i, a_p, m_p, and a_{can}. The overall shape of P_{can} does not change with i, a_p, m_p, and a_{can}. Figure 7*a* compares P_{can} for $i = 0.05$ and 0.07. The probability P_{can} for $i = 0.07$ is about two-thirds of P_{can} for $i = 0.05$. The decrease in P with increasing i is a feature common to P_{col}, P_{esc}, and P_{can}. Figure 7*b* compares P_{can} for $a_p = 5$ and 10 AU. The orbit-crossing region shifts outward and expands with a_p, and the maximum value of P_{can} increases with a_p. The maximum value of P_{can} for $a_p = 10$ AU is about twice that for $a_p = 5$ AU. Figure 7*c* compares P_{can} for $m_p = 1m_J$ and $0.3m_J$. The probability P_{can} for $m_p = 0.3m_J$ is about 1/10 of P_{can} for $m_p = 1m_J$. The value of P_{can} increases with m_p in a manner similar to P_{esc}.

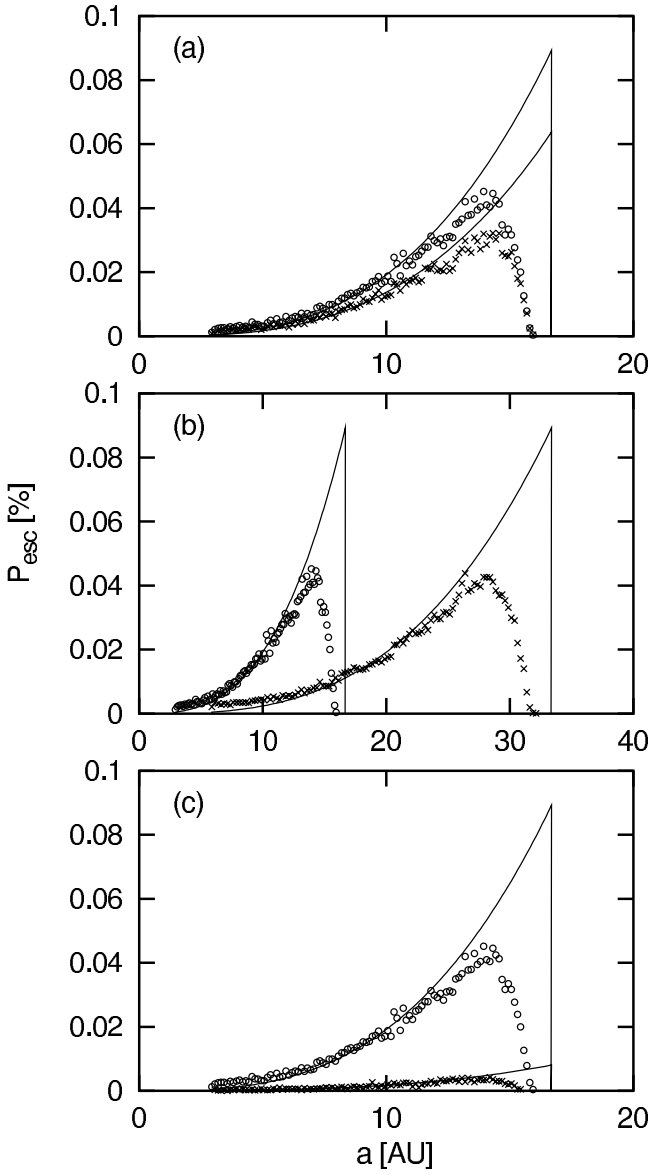

FIG. 5.—Probabilities $P_{\rm esc}$ for $e = 0.7$ in the standard case (*circles*) and various other cases (*crosses*) shown against a. Crosses in (*a*), (*b*), and (*c*) indicate $P_{\rm esc}$ in cases 6 ($i = 0.07$), 11 ($a_p = 10$ AU), and 14 ($m_p = 0.3 m_{\rm J}$), respectively. The solid curves show the empirical fits.

We plot $P_{\rm can}$ for $a_{\rm can} = 3000$ and 5000 AU in Figure 7*d*. The value of $P_{\rm can}$ decreases with increasing $a_{\rm can}$. For $a_{\rm can} = 5000$ AU, the probability $P_{\rm can}$ is about half of $P_{\rm can}$ for $a_{\rm can} = 3000$ AU.

3.4. *Two-dimensional Cases*

Figures 8, 9, and 10 show P against a for $i = 0$, i.e., cases 1, 13, and 19. Each panel compares P for different values of e, a_p, and m_p. In all panels the qualitative features of P are almost the same as for $i \neq 0$, but the values are higher. For example, in case 1, $P_{\rm col}$, $P_{\rm esc}$, and $P_{\rm can}$ for $i = 0$ are typically $\sim$100, $\sim$10, and $\sim$5 times higher than in the standard case, respectively. The parameter dependences of P, except on $a_{\rm can}$, are weaker than those in all cases for $i \neq 0$.

4. EMPIRICAL FITS FOR PROBABILITIES

We derive simple empirical formulae for P using the results of numerical integration, which is useful in estimating P for general planetary systems. For the empirical formulae for $P^{\rm fit}$, we use simple power-law fitting in a, e, i, a_p, m_p, and $a_{\rm can}$,

$$P^{\rm fit} = f a^{\alpha} e^{\beta} \sin i^{\gamma} a_p^{\delta} m_p^{\epsilon} a_{\rm can}^{\zeta}, \tag{5}$$

where f is a numerical factor and α, β, γ, δ, ϵ, and ζ represent power-law indices. The last term $a_{\rm can}^{\zeta}$ is only for candidacy. This assumption works well to reproduce the numerical results. By comparing $P^{\rm fit}$ with P, we estimate the values of f, α, β, γ, δ, ϵ, and ζ for collision, escape, and candidacy, and those for $i = 0$ empirically in simple figures. We adopt integers or simple fractions for their power-law indices. The empirical fits are sufficiently accurate for order-of-magnitude estimation of P. We plot $P^{\rm fit}$ in Figures 1 and 3–10 over the orbit-crossing region.

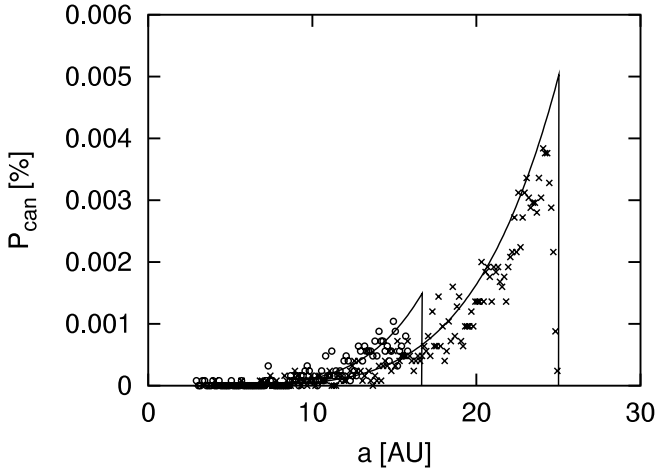

FIG. 6.—Probability $P_{\rm can}$ shown against a. Circles and crosses indicate $P_{\rm can}$ for $e = 0.7$ and 0.8, respectively, in the standard case [$(i, a_p, m_p, a_{\rm can}) = (0.05, 5\ {\rm AU}, 1 m_{\rm J}, 3000\ {\rm AU})$]. The solid curves show the empirical fits.

4.1. *Collision with a Planet*

By comparing equation (5) with $P_{\rm col}$ we obtain the empirical formula

$$P_{\rm col}^{\rm fit} \sim 7 \times 10^{-7} e^{-2} \sin i^{-1} \left(\frac{a_p}{\rm AU}\right)^{-1} \left(\frac{m_p}{m_{\rm J}}\right)^{4/3}, \tag{6}$$

where we approximate $P_{\rm col}$ as being constant in a, neglecting peaks at the ends of the orbit-crossing region. Although the fit of $P_{\rm col}^{\rm fit}$ does not reproduce the peaks at both ends of the orbit-crossing region, it approximates the average value of $P_{\rm col}$ for $0.1 \leq e \leq 0.9$. Equation (6) is valid in all cases for $i \neq 0$ in Table 1.

4.2. *Escape from a Planetary System*

We consider the cases for $e \geq 0.5$ and $m_p \leq 3 m_{\rm J}$, excluding cases 23 and 24, in which the simple fly-by theory is not valid. We replace e with $(1-e)$ in equation (5) because $P_{\rm esc}$ strongly depends on the perihelion distance $q = a(1 - e)$ rather than on e (e.g., Duncan et al. 1987).

By comparing equation (5) with $P_{\rm esc}$, we obtain

$$P_{\rm esc}^{\rm fit} \sim 4 \times 10^{-6} \left(\frac{a}{a_p}\right)^{3} (1 - e) \sin i^{-1} \left(\frac{m_p}{m_{\rm J}}\right)^{2}. \tag{7}$$

Comparing $P_{\rm esc}$ and equation (7) we find that the overall feature of $P_{\rm esc}$ for $i \neq 0$ is approximated by equation (7), except for

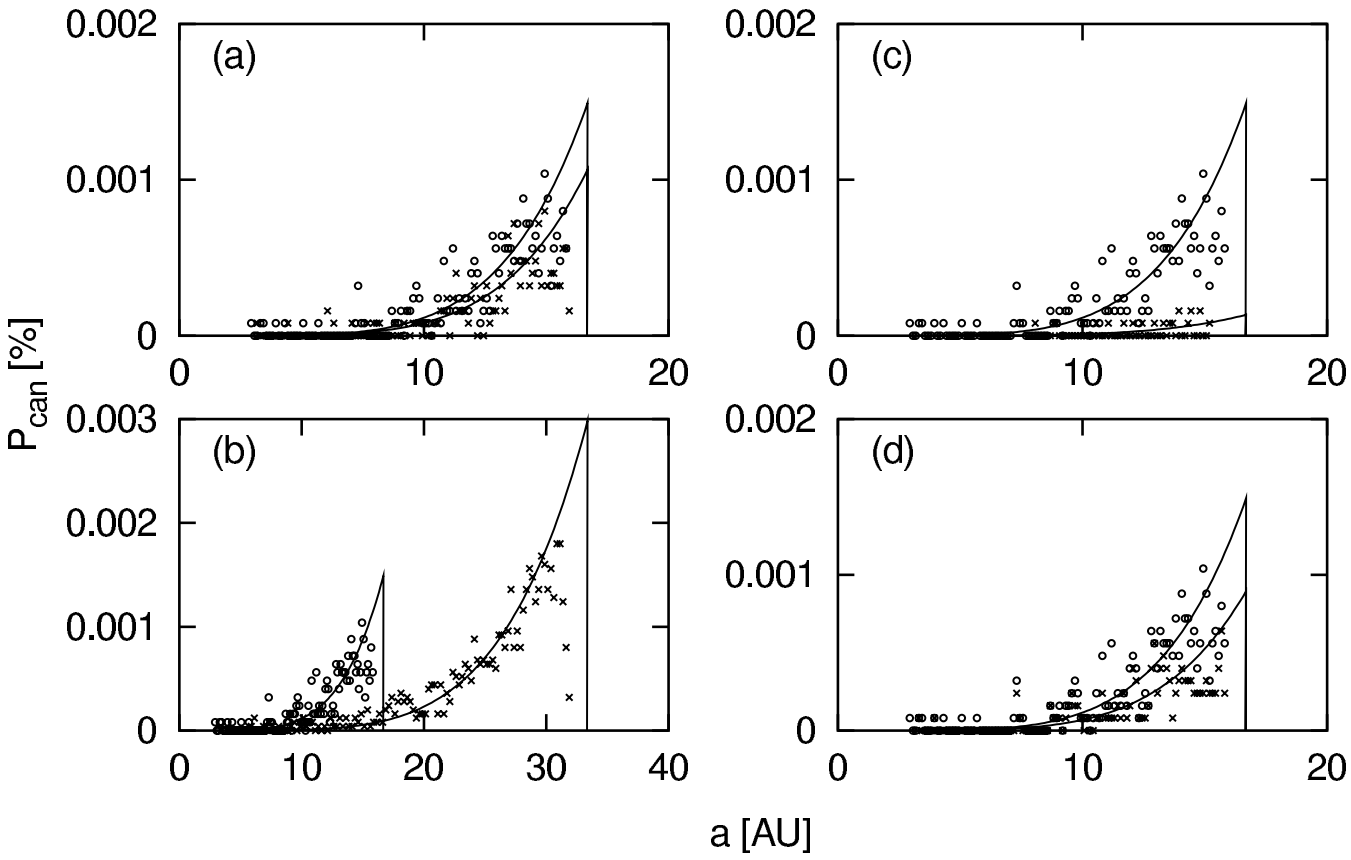

FIG. 7.—Probabilities $P_{\rm can}$ for $e = 0.7$ in the standard case for $a_{\rm can} = 3000$ AU (*circles*) and various other cases (*crosses*) shown against a. Crosses in (*a*), (*b*), (*c*), and (*d*) indicate $P_{\rm esc}$ in cases 6 ($i = 0.07$), 11 ($a_p = 10$ AU), 14 ($m_p = 0.3 m_{\rm J}$), and 0 ($a_{\rm can} = 5000$ AU), respectively. The solid curves show the empirical fits.

$e = 0.9$ in case 2 and for $e = 0.9$ in case 22. In these exceptional cases $P_{\rm esc}$ is roughly given by equation (10).

Note that $P_{\rm esc}^{\rm fit}$ reproduces only the increase in $P_{\rm esc}$ with a and overestimates $P_{\rm esc}$ for a after the rapid decrease around $a_{\rm max}$. The overestimation is due to the difference between the orbit-crossing region and the escape region. If these two regions are completely the same, there is almost no overestimation. However, the outer edge of the escape region, where $v_r > v_r^{\rm min}$, is smaller than the outer edge of the orbit-crossing region, $a_{\rm max}$. Since this difference is larger for smaller e, the overestimation of $P_{\rm esc}$ by $P_{\rm esc}^{\rm fit}$ is larger for smaller e. We find that $P_{\rm esc}^{\rm fit}$ agrees with the increase of $P_{\rm esc}$ with a for $e \geq 0.5$.

For a planetesimal with $a \gg a_p$, in other words, with $e \approx 1$, the energy change of planetesimals depends on a and e only through q (Duncan et al. 1987; Dones et al. 1996). Hence, under such conditions, equation (7) is no longer valid.

4.3. *Candidacy To Be a Member of a Comet Cloud*

The parameter ranges of e and m_p we consider here are $e \geq 0.4$ and $m_p \leq 3 m_{\rm J}$, and we replace e with $(1-e)$ in equation (5) for the same reason as for escape. By comparing equation (5) with $P_{\rm can}$, we obtain $P_{\rm can}^{\rm fit}$:

$$P_{\rm can}^{\rm fit} \sim 1.2 \times 10^{-5} \left(\frac{a}{a_p}\right)^5 (1-e)^2 \sin i^{-1} \left(\frac{m_p}{m_{\rm J}}\right)^2 \left(\frac{a_{\rm can}}{a_p}\right)^{-1}. \quad (8)$$

Equation (8) is in good agreement with the increase in $P_{\rm can}$ for $a_{\rm can} \gtrsim 10a$ and for $e \geq 0.6$. Similarly to $P_{\rm esc}^{\rm fit}$, $P_{\rm can}^{\rm fit}$ expresses only the increase in $P_{\rm can}$ with a but not the decrease around $a_{\rm max}$. We find that the behavior of $P_{\rm can}$ for $e = 0.9$ in cases 2, 3, and 22 is expressed by equation (11) rather than equation (8).

In previous studies, many authors mentioned Jupiter's inefficiency in forming candidates because of its high mass; however, we find that the ratio of $P_{\rm can}^{\rm fit}$ to $P_{\rm esc}^{\rm fit}$ does not depend on m_p from equations (7) and (8). For a planetesimal with $a \gg a_p$ or $e \approx 1$, equation (8) is not valid for the same reason as for escape (Duncan et al. 1987; Dones et al. 1996).

4.4. *Two-dimensional Cases*

We consider P in cases for $i = 0$. By comparing $P_{\rm col}$, $P_{\rm esc}$, $P_{\rm can}$, and $P^{\rm fit}$, we obtain $P_{\rm 2D}^{\rm fit}$:

$$P_{\rm 2D,col}^{\rm fit} \sim 8 \times 10^{-4} e^{-1} \left(\frac{a_p}{\rm AU}\right)^{-1/2} \left(\frac{m_p}{m_{\rm J}}\right)^{2/3}, \quad (9)$$

$$P_{\rm 2D,esc}^{\rm fit} \sim 2 \times 10^{-3} \left(\frac{a}{a_p}\right)^{3/2} (1-e)^{1/2} \left(\frac{m_p}{m_{\rm J}}\right), \quad (10)$$

$$P_{\rm 2D,can}^{\rm fit} \sim 3 \times 10^{-3} \left(\frac{a}{a_p}\right)^{7/2} (1-e)^{3/2} \left(\frac{m_p}{m_{\rm J}}\right) \left(\frac{a_{\rm can}}{a_p}\right)^{-1}. \quad (11)$$

As seen in Figures 8–10, equations (9)–(11) reproduce P well. We find that the ratio of $P_{\rm 2D,can}^{\rm fit}$ to $P_{\rm 2D,esc}^{\rm fit}$ also does not depend on m_p from equations (10) and (11).

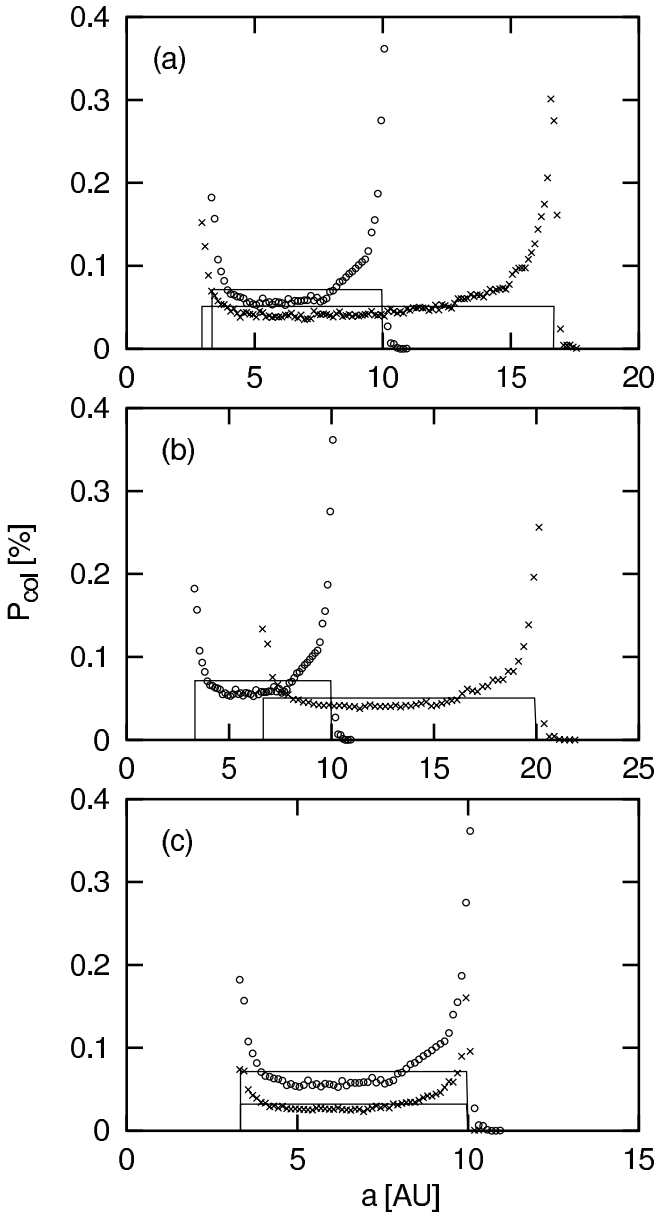

FIG. 8.—Probabilities P_{col} for $i = 0$ shown against a. Circles in all panels indicate P_{col} for $e = 0.5$ in the standard case. Crosses in (a), (b), and (c) indicate P_{col} for $e = 0.7$ in the standard case and cases 13 ($a_p = 10$ AU) and 19 ($m_p = 0.3m_J$), respectively. The solid lines show the empirical fits.

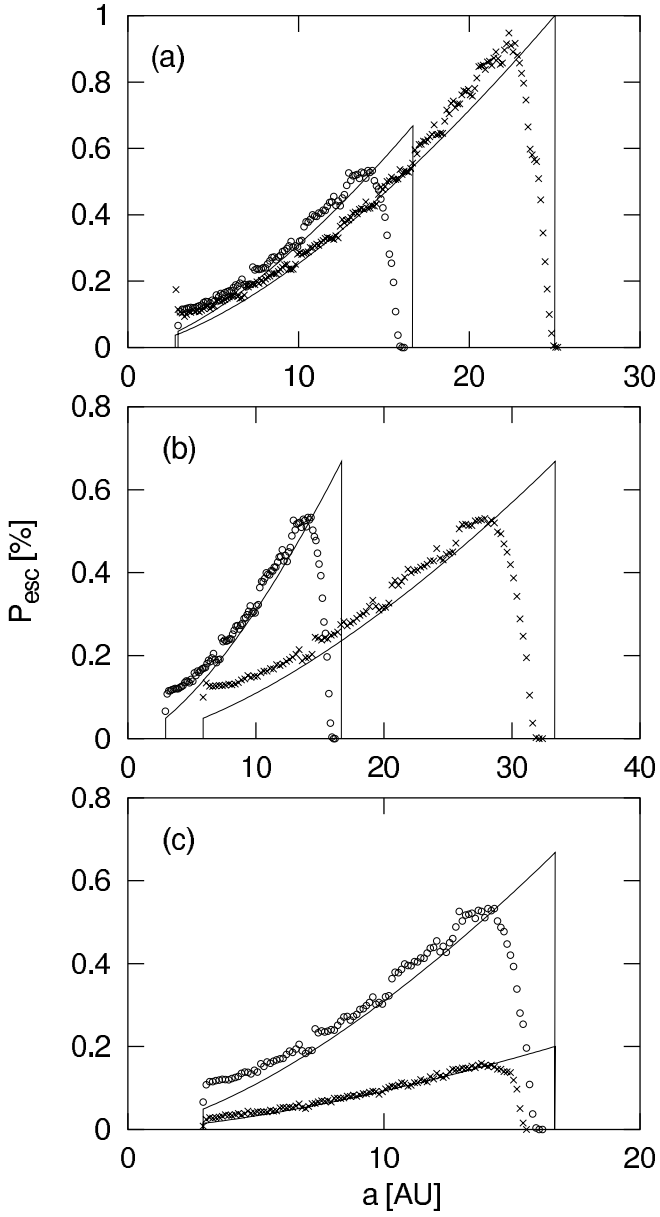

FIG. 9.—Probabilities P_{esc} for $i = 0$ shown against a. Circles in all panels indicate P_{esc} for $e = 0.7$ in the standard case. Crosses in (a), (b), and (c) indicate P_{esc} in the standard case for $e = 0.8$ and cases 13 ($a_p = 10$ AU) and 19 ($m_p = 0.3m_J$), respectively. The solid lines show the empirical fits.

4.5. *Geometric Interpretation*

In this section we try to understand the relation between P^{fit} and P^{fit}_{2D} using a geometric interpretation. We assume that the probability P^{fit} is approximated by the ratio of cross sections σ for collision, escape, and candidacy to the total cross section:

$$P^{fit} = \frac{\sigma}{\sigma_{total}}. \tag{12}$$

In $i \neq 0$ cases we define the total cross section as the cylindrical area at a_p through which planetesimals pass, which is estimated as

$$\sigma_{total} = 2\pi a_p 2a_p \sin i = 4\pi a_p^2 \sin i. \tag{13}$$

Using equation (12) and the P^{fit} obtained in §§ 4.1–4.3, we obtain σ:

$$\sigma_{col} \sim 8 \times 10^{-6} e^{-2} \left(\frac{a_p}{\mathrm{AU}}\right) \left(\frac{m_p}{m_J}\right)^{4/3}, \tag{14}$$

$$\sigma_{esc} \sim 5 \times 10^{-5} \left(\frac{a}{a_p}\right)^3 a_p^2 (1-e) \left(\frac{m_p}{m_J}\right)^2, \tag{15}$$

$$\sigma_{can} \sim 1.5 \times 10^{-4} \left(\frac{a}{a_p}\right)^5 a_p^2 (1-e)^2 \left(\frac{m_p}{m_J}\right)^2 \left(\frac{a_{can}}{a_p}\right)^{-1}. \tag{16}$$

In $i = 0$ cases P^{fit} is approximately given by the ratio of twice the impact parameter b to the length of the orbit of the planet:

$$P^{fit}_{2D} = \frac{b}{\pi a_p}. \tag{17}$$

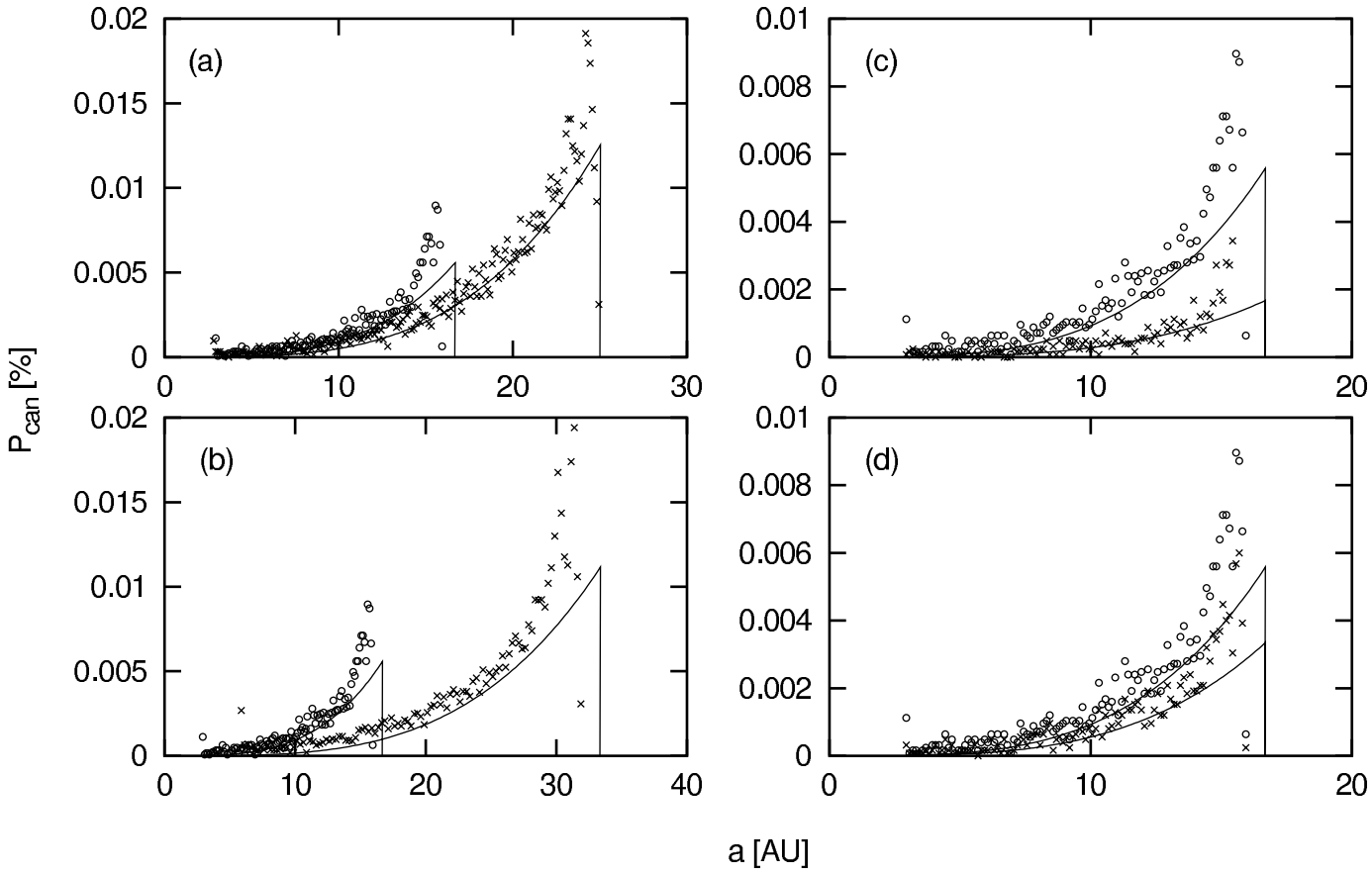

FIG. 10.—Probabilities $P_{\rm can}$ for $i = 0$ shown against a. Circles in all panels indicate $P_{\rm can}$ for $e = 0.7$ and $a_{\rm can} = 3000$ AU in the standard case. Crosses in (*a*), (*b*), (*c*), and (*d*) indicate $P_{\rm esc}$ in the standard case for $e = 0.8$ and in cases 13 ($a_p = 10$ AU), 19 ($m_p = 0.3 m_{\rm J}$), and 0 ($a_{\rm can} = 5000$ AU), respectively. The solid lines show the empirical fits.

Using equation (17) and $P_{\rm 2D}^{\rm fit}$ obtained in § 4.4, we obtain b:

$$b_{\rm col} \sim 2.5 \times 10^{-3} e^{-1} \left(\frac{a_p}{\rm AU}\right)^{1/2} \left(\frac{m_p}{m_{\rm J}}\right)^{2/3}, \quad (18)$$

$$b_{\rm esc} \sim 6 \times 10^{-3} \left(\frac{a}{a_p}\right)^{3/2} (1-e)^{1/2} a_p \left(\frac{m_p}{m_{\rm J}}\right), \quad (19)$$

$$b_{\rm can} \sim 9 \times 10^{-3} \left(\frac{a}{a_p}\right)^{7/2} (1-e)^{3/2} a_p \left(\frac{m_p}{m_{\rm J}}\right) \left(\frac{a_{\rm can}}{a_p}\right)^{-1}. \quad (20)$$

The power-law index of $b_{\rm col}$ for m_p, $\epsilon_{\rm col} = 2/3$, reflects that gravitational focusing is effective (e.g., Kokubo & Ida 1996). The dependences of $b_{\rm esc}$ and $b_{\rm can}$ on m_p are the same as that of r_g on m_p.

From equations (14)–(16) and (18)–(20) we find the relations $\sigma \sim \pi b^2$ for collision and escape and $\sigma \sim 2\pi b_{\rm esc} b_{\rm can}$ for candidacy. These relations suggest that $b_{\rm col}$, $b_{\rm esc}$, and $b_{\rm can}$ can be interpreted as the effective maximum impact parameters. The cross sections for collision and escape, $\sigma_{\rm col}$ and $\sigma_{\rm esc}$, are roughly given by circular areas with radii of $b_{\rm col}$ and $b_{\rm esc}$, respectively. The cross section of candidacy is consistently approximated as a narrow ring area with a width $b_{\rm can}$ and a radius $b_{\rm esc}$ just outside of $\sigma_{\rm esc}$. Note that the actual shape of σ is not a circle or a ring but rather a complicated figure. However, the geometric interpretation with the effective impact parameters is almost consistent with the numerical results in both the $i \neq 0$ and $i = 0$ cases.

In equation (12) we assume $\sigma_{\rm total}$ includes σ. However, the width of the total cross section $a_p \sin i$ decreases with i and becomes smaller than the width of σ ($2b$) for small i. Then the behavior of P for $i \neq 0$ becomes similar to that for $P_{\rm 2D}^{\rm fit}$ rather than for $P^{\rm fit}$. We can roughly estimate the parameter ranges in which $P_{\rm col}^{\rm fit}$ and $P_{\rm esc}^{\rm fit}$ are valid from the condition $b \leq a_p \sin i$, which leads to

$$\left(\frac{m_p}{m_{\rm J}}\right) \lesssim 2 \times 10^2 \left(\frac{e}{0.5}\right)^{3/2} \left(\frac{a_p}{5\ {\rm AU}}\right)^{3/4} \left(\frac{\sin i}{\sin 0.05}\right)^{3/2}, \quad (21)$$

$$\left(\frac{m_p}{m_{\rm J}}\right) \lesssim 4 \left(\frac{1-e}{0.3}\right) \left(\frac{\sin i}{\sin 0.05}\right), \quad (22)$$

where we use $b = (\sigma/\pi)^{1/2}$, which is about 50% smaller than the value of b of equation (18) or (19). The criterion for $P_{\rm can}^{\rm fit}$ to be valid is $b_{\rm esc} + b_{\rm can} < a_p \sin i$. This criterion reduces to the same criterion as for $P_{\rm esc}^{\rm fit}$ (eq. [22]) because $b_{\rm can} \ll b_{\rm esc}$. However, $P_{\rm can}^{\rm fit}$ is more sensitive to the criterion than $P_{\rm esc}$ because $\sigma_{\rm can}$ is the area outside of $\sigma_{\rm esc}$. These criteria are all consistent with the results of the numerical calculations, as we mention in §§ 4.1–4.3.

5. EFFICIENCIES

We calculate the efficiencies of collision, escape, and candidacy from equation (2) and the numerical results for P. To obtain realistic efficiencies we need to know the orbital distribution

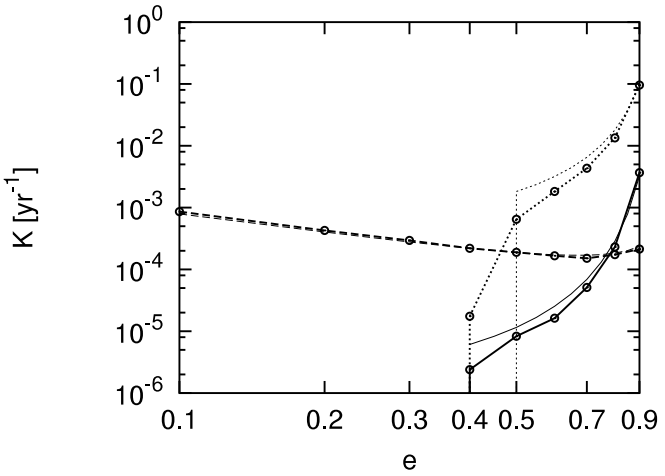

FIG. 11.—Efficiencies $K_{\rm col}$ (*dashed line*), $K_{\rm esc}$ (*dotted line*), and $K_{\rm can}$ (*solid line*) plotted against e in the standard case [$(i,\ a_p,\ m_p,\ a_{\rm can}) = (0.05,\ 5\ {\rm AU},\ 1m_{\rm J},\ 3000\ {\rm AU})$] for $\theta = 0$. The curves without symbols show the empirical fits.

of planetesimals around a planet during or after planet formation. However, this distribution is uncertain so far. In the present paper, as the first step, we adopt simple disk models: (1) flat disk ($\theta = 0$), (2) standard disk ($\theta = -3/2$), and (3) standard disk with a solar system planet. In model 3 we consider the four giant planets of the solar system. We use $n_1 = 1$ in the disk models for simplicity. We also obtain empirical fits of the efficiency $K^{\rm fit}$ from equation (2) and $P^{\rm fit}$. The empirical fits $K^{\rm fit}$ are shown with K in Figures 11–13. We plot $K_{\rm col}^{\rm fit}$ for $0.1 \le e \le 0.9$, $K_{\rm esc}^{\rm fit}$ for $e \ge 0.5$, and $K_{\rm can}^{\rm fit}$ for $e \ge 0.4$.

5.1. *Flat Disk*

Figure 11 shows K against e in the standard case $\theta = 0$, $a_{\rm in} = 0$, and $a_{\rm out} = \infty$. The collision probability $K_{\rm col}$ decreases gradually with increasing e. On the other hand, for $e \ge 0.4$, $K_{\rm esc}$ and $K_{\rm can}$ increase monotonically with e. As we have already seen in §§ 4.2 and 4.3, $K_{\rm esc}$ and $K_{\rm can}$ are positive only for $e \ge 0.4$. The relative magnitude between $K_{\rm col}$ and $K_{\rm esc}$ or $K_{\rm can}$ varies with e. Only $K_{\rm col}$ has a positive value for $e \le 0.3$. For $e \ge 0.5$, $K_{\rm esc}$ is larger than both $K_{\rm col}$ and $K_{\rm can}$, and $K_{\rm can}$ exceeds $K_{\rm col}$ for $e \ge 0.8$. The dependences of K on i, m_p, and $a_{\rm can}$ are independent of θ and the same as for P.

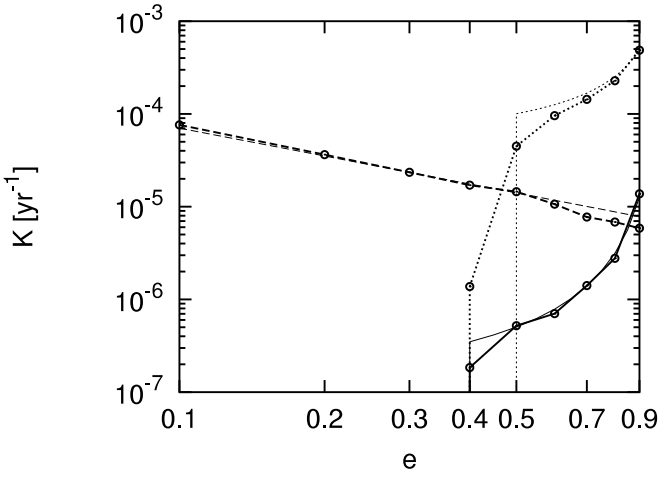

FIG. 12.—Same as Fig. 11, but for $\theta = -3/2$.

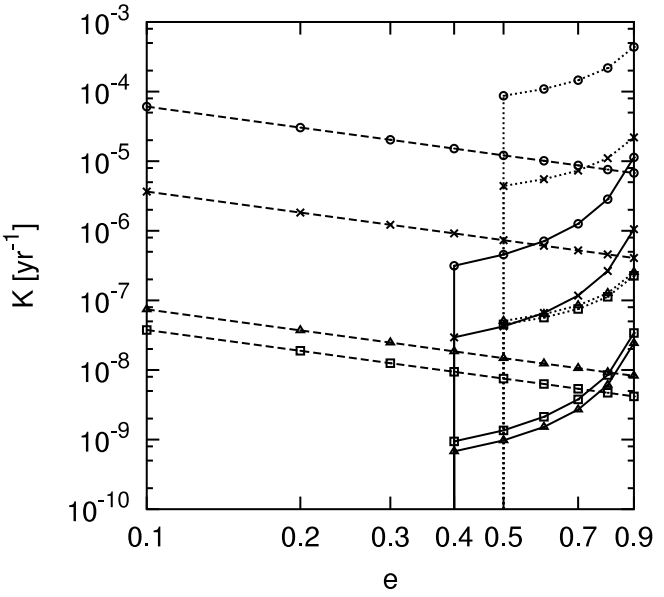

FIG. 13.—Efficiencies $K_{\rm col}^{\rm fit}$ (*dashed line*), $K_{\rm esc}^{\rm fit}$ (*dotted line*), and $K_{\rm can}^{\rm fit}$ (*solid line*) shown against e in the cases for Jupiter [$(a_p,\ m_p) = (5.2\ {\rm AU},\ 0.95m_{\rm J})$; *circles*], Saturn [$(a_p,\ m_p) = (9.6\ {\rm AU},\ 0.29m_{\rm J})$; *crosses*], Uranus [$(a_p,\ m_p) = (19.2\ {\rm AU},\ 0.044m_{\rm J})$; *triangles*], and Neptune [$(a_p,\ m_p) = (30.1\ {\rm AU},\ 0.052m_{\rm J})$; *squares*] for $i = 0.05$ and $a_{\rm can} = 3000$ AU.

The empirical formulae $K^{\rm fit}$ integrated over the orbit-crossing region for $\theta = 0$ are

$$K_{\rm col}^{\rm fit} \sim 9\times10^{-6}e^{-2}\left[(1-e)^{-1/2} - (1+e)^{-1/2}\right] \times \sin^{-1} i \left(\frac{a_p}{\rm AU}\right)^{-1/2}\left(\frac{m_p}{m_{\rm J}}\right)^{4/3}, \quad (23)$$

$$K_{\rm esc}^{\rm fit} \sim 7\times10^{-6}(1-e)^{-5/2}\sin^{-1} i \left(\frac{a_p}{\rm AU}\right)^{1/2}\left(\frac{m_p}{m_{\rm J}}\right)^{2}, \quad (24)$$

$$K_{\rm can}^{\rm fit} \sim 1.4\times10^{-5}(1-e)^{-7/2}\sin^{-1} i \left(\frac{a_p}{\rm AU}\right)^{3/2}\left(\frac{m_p}{m_{\rm J}}\right)^{2}\left(\frac{a_{\rm can}}{\rm AU}\right)^{-1}, \quad (25)$$

where we neglect the terms of $(1 + e)$ with power-law indices smaller than $-\frac{1}{2}$. These empirical fits are also plotted in Figure 11. The fit of $K_{\rm col}^{\rm fit}$ shows good agreement with $K_{\rm col}$. The differences are within ~10% for all e. For $e = 0.5$, $K_{\rm esc}^{\rm fit}$ agrees with $K_{\rm esc}$ within a factor of ~3. For $e \ge 0.6$, $K_{\rm esc}^{\rm fit}$ agrees with $K_{\rm esc}$ within ~70% error. The fit of $K_{\rm can}^{\rm fit}$ agrees with $K_{\rm can}$ within a factor of ~3 for $e = 0.4$ and within ~50% error for $e \ge 0.5$. These errors of $K_{\rm esc}^{\rm fit}$ and $K_{\rm can}^{\rm fit}$ decrease with increasing e because the regions where escapers and candidates appear overlap well with the orbit-crossing region for large e, as shown in Figures 4 and 6.

We also compare K and $K^{\rm fit}$ in other cases and find that K is well approximated by $K^{\rm fit}$. Their errors are typically about the same as for the standard case. In the worst cases $K^{\rm fit}$ agrees with K within ~50% for collision for $0.1 \le e \le 0.9$ and within a factor of ~3 for escape for $e \ge 0.5$, except for case 16. In the worst cases for candidacy $K_{\rm can}^{\rm fit}$ agrees with K within a factor of ~5 for $e = 0.4$ and ~2 for $e \ge 0.5$, except for case 16.

The relative magnitude of K also varies with a_p and m_p. Using equations (23)–(25) we can derive the dependences of the ratios as $K_{\rm esc}/K_{\rm col} \propto a_p m_p^{2/3}$ for $e \ge 0.4$ and $K_{\rm can}/K_{\rm col} \propto a_p^2 m_p^{2/3} a_{\rm can}^{-1}$ for

$e \geq 0.5$. These relations imply that planets with large semimajor axes and/or large mass produce escapers and candidates effectively compared to the production of colliders.

5.2. *Standard Disk*

Figure 12 shows K against e in the standard case and for $\theta = -3/2$, which is the standard value for protoplanetary disks (Hayashi 1981). The integration range is from $a_{\rm in} = 0$ to $a_{\rm out} = \infty$. The dependences of $K_{\rm col}$, $K_{\rm esc}$, and $K_{\rm can}$ on e are stronger than for the flat disk model. The relations among $K_{\rm col}$, $K_{\rm esc}$, and $K_{\rm can}$ are almost the same as for the flat disk model. The efficiencies $K_{\rm esc}$ and $K_{\rm can}$ exceed $K_{\rm col}$ at $e = 0.5$ and $e = 0.9$, respectively.

The empirical formulae $K^{\rm fit}$ for $\theta = -3/2$ are

$$K_{\rm col}^{\rm fit} \sim 9 \times 10^{-6} e^{-1} \sin^{-1} i \left(\frac{a_p}{\rm AU}\right)^{-2} \left(\frac{m_p}{m_{\rm J}}\right)^{4/3}, \quad (26)$$

$$K_{\rm esc}^{\rm fit} \sim 1.3 \times 10^{-5} (1-e)^{-1} \sin^{-1} i \left(\frac{a_p}{\rm AU}\right)^{-1} \left(\frac{m_p}{m_{\rm J}}\right)^{2}, \quad (27)$$

$$K_{\rm can}^{\rm fit} \sim 1.9 \times 10^{-5} (1-e)^{-2} \sin^{-1} i \left(\frac{m_p}{m_{\rm J}}\right)^{2} \left(\frac{a_{\rm can}}{\rm AU}\right)^{-1}. \quad (28)$$

These empirical fits are plotted in Figure 12.

The fit of $K_{\rm col}^{\rm fit}$ agrees well with $K_{\rm col}$ within $\sim$10% error for $e \leq 0.6$. For $e \geq 0.7$ the errors are larger and within $\sim$40%. The fit of $K_{\rm esc}^{\rm fit}$ agrees with $K_{\rm esc}$ within a factor of $\sim$2 for $e = 0.5$ and within $\sim$30% error for $e \geq 0.5$. The fit of $K_{\rm can}^{\rm fit}$ agrees with $K_{\rm can}$ within a factor of $\sim$2 for $e = 0.4$. For $e \geq 0.5$, $K_{\rm can}^{\rm fit}$ and $K_{\rm can}$ show good agreement within $\sim$15% error. Compared with the flat disk model, the errors between K and $K^{\rm fit}$ of escape and candidacy are small. This is because the contributions of P at large a, where the differences between P and $P^{\rm fit}$ are large, are weakened for small θ.

The efficiencies in other cases are also approximated by $K^{\rm fit}$, with errors similar to the standard case. In the worst cases $K^{\rm fit}$ agrees with K within $\sim$50% error for collision for $0.1 \geq e \geq 0.9$ and within a factor of $\sim$3 for escape for $e \geq 0.5$. In the worst cases for candidacy, $K_{\rm can}^{\rm fit}$ expresses $K_{\rm can}$ within a factor of $\sim$4 for $e = 0.4$ and $\sim$2 for $e \geq 0.5$.

5.3. *Application to the Solar System*

We apply the results of P to the solar system and compare the K-value of the four giant planets, Jupiter, Saturn, Uranus, and Neptune, using the empirical fits $K_{\rm col}^{\rm fit}$, $K_{\rm esc}^{\rm fit}$, and $K_{\rm can}^{\rm fit}$. We use the present values of a_p and m_p and assume the eccentricities of the planets as $e_p = 0$. We adopt $\theta = -3/2$, which corresponds to the standard protoplanetary disk for the solar system. The integration range is from $a_{\rm in} = 0$ to $a_{\rm out} = \infty$.

Figure 13 shows $K_{\rm col}^{\rm fit}$, $K_{\rm esc}^{\rm fit}$, and $K_{\rm can}^{\rm fit}$ for the giant planets against e for $i = 0.05$ and $a_{\rm can} = 3000$ AU. Jupiter always has the highest $K^{\rm fit}$ because of having the largest m_p. Among the four planets, the inner planets have higher $K_{\rm col}^{\rm fit}$, and the massive planets have higher $K_{\rm can}^{\rm fit}$. For escape, Uranus and Neptune have almost the same values of $K_{\rm esc}^{\rm fit}$. The relative magnitudes between $K_{\rm col}^{\rm fit}$ and $K_{\rm esc}^{\rm fit}$ and those between $K_{\rm esc}^{\rm fit}$ and $K_{\rm can}^{\rm fit}$ do not vary with the planets. All $K_{\rm esc}^{\rm fit}$ values exceed $K_{\rm col}^{\rm fit}$ and $K_{\rm can}^{\rm fit}$ for $e \geq 0.5$. Only the relative magnitudes between $K_{\rm col}^{\rm fit}$ and $K_{\rm can}^{\rm fit}$ vary slightly with the planets. For Jupiter, Saturn, and Uranus $K_{\rm can}^{\rm fit}$ exceeds $K_{\rm col}^{\rm fit}$ for $e = 0.9$. For Neptune $K_{\rm can}^{\rm fit}$ exceeds $K_{\rm col}^{\rm fit}$ for $e \geq 0.8$.

Next we consider the case in which i is proportional to the reduced Hill radius of the planet: $h = r_{\rm H}/a_p$. For each planet we set the inclination of the planetesimals to $i = h$. This application reflects that planetesimals around a planet are excited to the degree that $i \propto h$ (Ida & Makino 1993). Figure 14 shows $K_{\rm col}^{\rm fit}$, $K_{\rm esc}^{\rm fit}$, and $K_{\rm can}^{\rm fit}$ for the giant planets against e for $i = h$ and $a_{\rm can} = 3000$ AU. The relative importance of the planets in each $K^{\rm fit}$ and the relation among $K^{\rm fit}$ values for a planet are almost the same as for $i = 0.05$. Compared to the case for $i = 0.05$, $K^{\rm fit}$ slightly decreases for Jupiter because for Jupiter $i > 0.05$. For other planets, as $i < 0.05$, $K^{\rm fit}$ increases. In this model Jupiter still has the highest $K^{\rm fit}$, despite the disadvantage of having the highest i among the four planets.

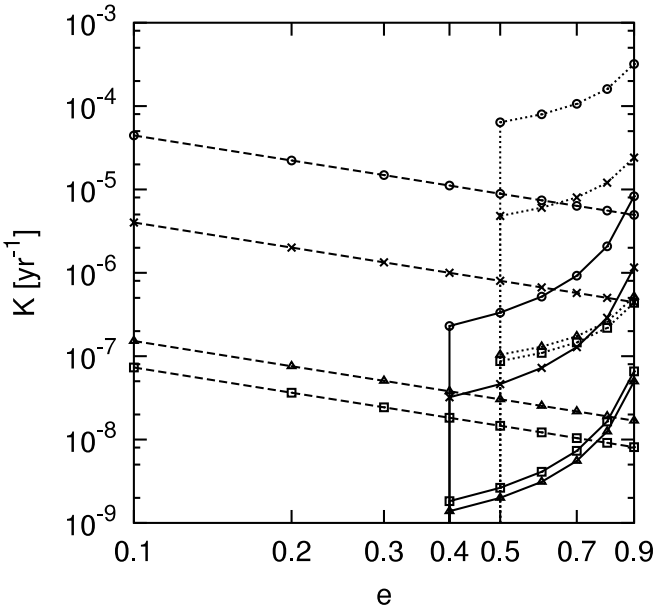

FIG. 14.—Efficiencies $K_{\rm col}^{\rm fit}$ (*dashed line*), $K_{\rm esc}^{\rm fit}$ (*dotted line*), and $K_{\rm can}^{\rm fit}$ (*solid line*) shown against e in the cases for Jupiter [$(i,\ a_p,\ m_p) = (0.0683,\ 5.2$ AU, $0.95 m_{\rm J})$; *circles*], Saturn [$(i,\ a_p,\ m_p) = (0.0457,\ 9.6$ AU, $0.29 m_{\rm J})$; *crosses*], Uranus [$(i,\ a_p,\ m_p) = (0.0244,\ 19.2$ AU, $0.044 m_{\rm J})$; *triangles*], and Neptune [$(i,\ a_p,\ m_p) = (0.0258,\ 30.1$ AU, $0.052 m_{\rm J})$; *squares*] for $a_{\rm can} = 3000$ AU.

In the real solar system planets have finite e_p; thus, the results of circular restricted three-body formalism may not be directly applicable. However, the e_p values of the four giant planets are small ($e_p \simeq 0.05$) and do not make any large differences in K. We perform calculations in the standard case with $e_p = 0.05$ and find that the difference between K-values for $e_p = 0$ and 0.05 is less than 10% for collision and less than 3% for escape. For candidacy the difference is typically within $\sim$5%, with a maximum difference of $\sim$25%.

6. SUMMARY AND DISCUSSION

We performed numerical calculations of the first dynamical stage of comet cloud formation, scattering of planetesimals by a planet. The orbital evolution of planetesimals was investigated using circular restricted three-body formalism. We considered planets of $m_p = (0.1\text{–}10) m_{\rm J}$ and $a_p = 1\text{–}30$ AU and planetesimals of $e = 0.1\text{–}0.9$ and $i = 0\text{–}0.1$.

We obtained the probabilities P of collision with a planet, escape from a planetary system, and candidacy for inclusion in a comet cloud for a single encounter as functions of orbital parameters of planets and planetesimals. We found that a planetesimal with an initial eccentricity of $e \gtrsim 0.4$ can escape from the planetary system or be a candidate for the comet cloud due to scattering by a planet. The probability of any planet producing escapers is always much higher than that of producing

candidates, since the energy range of the comet cloud is narrow. Furthermore, the production ratio of candidates to escapers is independent of m_p. We also derived simple empirical formulae for these probabilities that are accurate enough to use for order-of-magnitude estimation. Using the probabilities and assuming the distribution of planetesimals, we obtained the efficiencies K of planets for collision, escape, and candidacy.

We applied the results to the giant planets in the solar system and the standard disk model for solar system formation. We found that among the four giant planets, Jupiter is most responsible for producing candidates for elements of the Oort Cloud insofar as the inclination of planetesimals is constant or proportional to the reduced Hill radius of each planet.

Simulations in Dones et al. (2006) showed that the typical comet in the Oort Cloud is a planetesimal originally from the Uranus-Neptune region, placed in the Oort Cloud by Saturn. Dones et al. (2006) calculated the efficiency η for each planet, which is the ratio of the number of planetesimals remaining in the Oort Cloud to that of planetesimals that had close encounters with the planet after 4 Gyr. The efficiencies for Jupiter and Saturn are $\sim$2% and are about 1/10 of those for Uranus or Neptune. They concluded that Jupiter and Saturn eject from the solar system many planetesimals that had close encounters with them and that their efficiencies for populating the Oort Cloud are low compared to those for Uranus and Neptune. On the other hand, what we evaluate as $P_{\rm can}$ is the probability of the formation of candidates from among all planetesimals with a certain e and i and on crossing orbits with a planet, taking into account not only close encounters with the planet but also distant encounters. Our results show that under the same conditions for planetesimals, Jupiter has the highest $P_{\rm can}$ among the four planets, or the highest potential ability to form candidates.

In this paper we investigated the elementary process of scattering of planetesimals by a planet and applied the results to simple planetesimal disk models. In order to construct a more realistic formation scenario of a comet cloud, we have to clarify the number and orbital distributions of planetesimals around planets during and just after planet formation. The distributions are affected by the structure of planetary systems, the interactions among planetesimals, and the existence of the gas disk. By applying our results to the realistic distributions of planetesimals, we will be able to discuss a more realistic scenario of comet cloud formation.

This work was partially supported by the Ministry of Education, Culture, Sports, Science, and Technology, Japan, the 21st Century COE Program ''Origin and Evolution of Planetary Systems'' and a Grant-in-Aid for Scientific Research on Priority Areas, ''Development of Extrasolar Planetary Science.'' A. H. is supported by a Japan Society for the Promotion of Science Research Fellowship for Young Scientists. We wish to thank E. I. Chiang for his useful comments. We would also like to thank the anonymous referee for valuable comments and suggestions.

REFERENCES

Bertotti, B., Farinella, P., & Vokrouhlický, D. 2003, Physics of the Solar System (Dordrecht: Kluwer)
Dones, L., Levison, H. F., & Duncan, M. 1996, in ASP Conf. Ser. 107, Completing the Inventory of the Solar System, ed. T. W. Rettig & J. M. Hahn (San Francisco: ASP), 233
Dones, L., Levison, H. F., Duncan, M., & Weissman, P. 2006, Icarus, in press
Dones, L., Weissman, P., Levison, H. F., & Duncan, M. 2004, in Comets II, ed. M. C. Festou, H. U. Keller, & H. A. Weaver (Tucson: Univ. Arizona), 153
Duncan, M., Quinn, T., & Tremaine, S. 1987, AJ, 94, 1330
Fernández, J. A. 1978, Icarus, 34, 173
Hayashi, C. 1981, Prog. Theor. Phys. Suppl., 70, 35
Heisler, J., & Tremaine, S. 1986, Icarus, 65, 13
Ida, S., & Makino, J. 1993, Icarus, 106, 210
Kokubo, E., & Ida, S. 1996, Icarus, 123, 180
Madonna, R. G. 1997, Orbital Mechanics (Malabar: Krieger)
Makino, J. 1991, PASJ, 43, 859
Makino, J., & Aarseth, S. J. 1992, PASJ, 44, 141
Oort, J. H. 1950, Bull. Astron. Inst. Netherlands, 11, 91
Safronov, V. S. 1972, IAU Circ., 45, 329
Tremaine, S. 1993, in ASP Conf. Ser. 36, Planets around Pulsars, ed. J. A. Phillips, S. E. Thorsett, & S. R. Kulkarni (San Francisco: ASP), 335
Weidenschilling, S. J. 1975, AJ, 80, 145
Weissman, P. R. 1990, Nature, 344, 825